
RESILIENT CONTROLLER DESIGN WITH EXPONENTIAL REACHING LAW FOR ENHANCED LOAD FREQUENCY STABILITY IN MULTI-AREA INTERCONNECTED MICROGRIDS

Md Saiful Islam, Rahul Bhadani
 AI, Autonomy, Resilience, Control (AARC) Lab
 Electrical & Computer Engineering
 The University of Alabama in Huntsville
 301 Sparkman Drive, Huntsville, AL 35899, USA
 mil499@uah.edu, rahul.bhadani@uah.edu

ABSTRACT

We present a load frequency control strategy deploying a decentralized robust global integral terminal sliding mode control (GITSMC) method to maintain stable frequency and tie-line power in multi-area interconnected microgrids with aggregated uncertainties. To achieve this, firstly, we have developed a mathematical model of the multi-area interconnected system incorporating disturbances from solar photovoltaic (PV), wind turbine (WT) generation and load demand, as aggregated uncertainties. Secondly, we have designed a global integral terminal sliding surface with an exponential reaching law for each area to enhance system dynamic performance and suppress chattering within a finite time. Thirdly, the overall stability of the closed-loop system is analyzed using the Lyapunov stability theorem. Finally, extensive simulations are conducted on the IEEE 10-generator New England 39-bus power system, including load disturbances and variable PV and WT generation. The results demonstrate the performance of the proposed GITSMC approach, achieving approximately 94.9% improvement in ITSE and 94.4% improvement in ISE, confirming its superior accuracy and dynamic performance compared to the existing controller.

Keywords Load frequency control · Multi-area interconnected microgrid · Global integral terminal sliding mode control · Exponential reaching law · Lyapunov stability

1 Introduction

Rising concerns over climate change and fossil fuel depletion have accelerated the global shift toward renewable-based power systems. Wind turbine (WT) and photovoltaic (PV) power generation, being clean and sustainable, play a major role in electric power production [1, 2, 3]. However, their intermittent and weather-dependent nature introduces notable voltage and frequency variations [4]. In large interconnected grids, high renewable penetration intensifies operational uncertainty, reduces system inertia, and heightens vulnerability to generation-load imbalances [5]. These fluctuations can cause significant frequency deviations, leading to grid destabilization. Although primary control actions, such as turbine governors, respond to disturbances, they often fail to eliminate steady-state errors or suppress oscillations. Therefore, the load frequency control (LFC) is required to maintain stable tie-line (transmission line connecting two or more power systems [6]) power and frequency. Recent research emphasizes robust LFC strategies to enhance transient stability [7, 8] in renewable-integrated multi-area interconnected microgrids (MAIMGs) as presented in Figure 1. When several geographically dispersed AC and DC microgrid systems are linked together through interconnections, they collectively form what is known as a **multi-area interconnected microgrid** [9].

The sliding mode controller (SMC) has attracted attention for its robustness in LFC under parameter variations and external disturbances. A robust H_∞ based SMC was proposed in [10] for MAIMGs, addressing time-delay disturbances. However, unmodeled dynamics and external disturbances were not considered. To overcome this, an extended disturbance observer-based SMC was introduced in [11], treating tie-line and load variations as disturbances.

Yet, parameter variations and renewable generation impacts remained unaddressed. To address these, [12] proposed an observer-based fractional-order SMC for hybrid wind–diesel systems, though the use of a discontinuous signum function caused oscillations, limiting practical feasibility.

Fractional-order terminal SMC achieves uniform voltage regulation under wide load and input variations [13], while global fast terminal SMC improves convergence by adding linear terms, enhancing dynamic response [14]. Adaptive TSMC integrated with energy storage was proposed in [15], but its effectiveness under mismatched disturbances from intermittent renewable sources was not evaluated. Similarly, [16] did not fully analyze the effects of disturbances induced by renewable sources. Moreover, the widespread deployment of energy storage faces design complexities and higher costs. To address these limitations, [17] suggested a robust, chattering-free adaptive higher-order integral SMC for hydro-based LFC, but neglecting other renewable sources like solar PV and WT is impractical. Higher-order integral SMCs also involve complex stability proofs and higher-order derivatives, increasing noise. Integral terminal SMC improves convergence, reduces chattering, and enhances dynamics [1].

Building upon the benchmark multi-area LFC models established in [18, 19, 20, 21], this paper proposes a robust decentralized global integral terminal sliding mode controller (GITSMC) to achieve improved tie-line power and frequency regulation in multi-area interconnected systems with integrated WT and PV power generation.

The main contributions are as follows:

1. Development of a multi-area interconnected LFC model incorporating solar and wind sources, considering parametric uncertainty and external disturbances as lumped uncertainties.
2. Design of a decentralized robust GITSMC in conjunction with an exponential reaching law that suppresses chattering, avoids singularity while minimizing steady-state error, and ensures fast finite-time convergence.
3. Comparative analysis with the classical proportional-integral (PI) controller, demonstrating the superior performance of the proposed controller.
4. Validation on the IEEE 10 generators 39-bus New England power system under varying generation and load conditions.

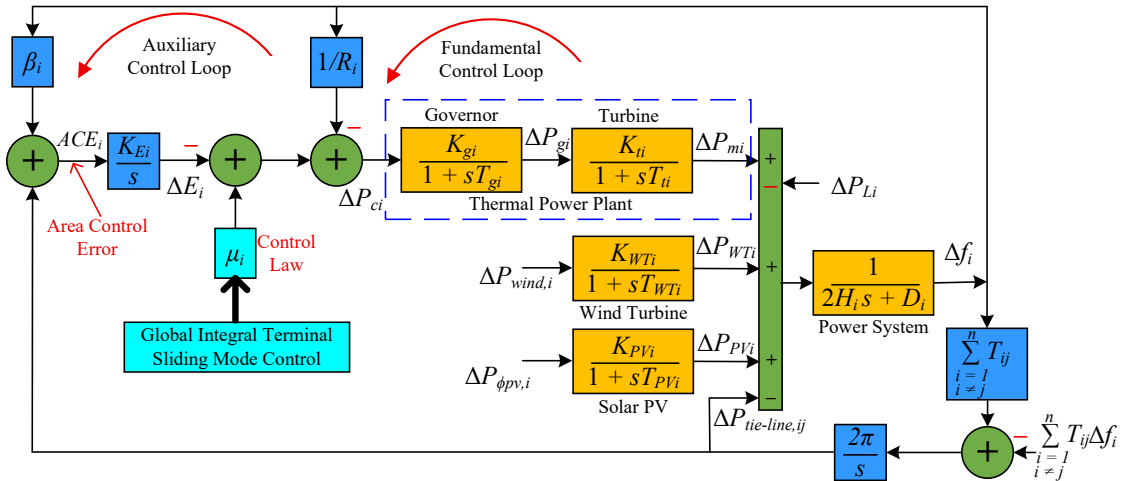


Figure 1: Multi-area interconnected microgrids with thermal power plant along with PV and wind generators.

2 Modeling of Multi-Area Interconnected Microgrids

Figure 1 illustrates the i^{th} area of an interconnected power system comprising a PV power generator, a thermal power plant, a wind power generator, and loads. The tie-line power deviation (ΔP_{tie-ij}) and the frequency deviation (Δf_i) are adjusted by controlling the mechanical output power (ΔP_{mi}) in response to load (ΔP_{Li}), solar PV (ΔP_{PVi}), wind (ΔP_{WTi}), and tie-line power variations, utilizing the speed governor in the primary control loop. Since the primary controller cannot fully restore frequency, a decentralized robust GITSMC is proposed to mitigate tie-line power as well

as frequency deviations. For simplicity, the i^{th} area is modeled as [19, 20, 21, 22]:

$$\begin{aligned}
\Delta \dot{P}_{\text{tie-ij}} &= 2\pi \left(\sum_{i=1, i \neq j}^n T_{ij} (\Delta f_i(t) - \Delta f_j(t)) \right) \\
\Delta \dot{f}_i &= f_i(t) + P_{mi}(t) + P_{PV_i} + P_{WT_i}(t) + P_{tie-ij}(t) + P_{Li}(t) \\
\Delta \dot{P}_{mi} &= -\frac{K_{ti}}{T_{ti}} (\Delta P_{mi}(t) - \Delta P_{gi}(t)) \\
\Delta \dot{E}_i &= K_{Ei} (\beta_i \Delta f_i(t) + \Delta P_{\text{tie-ij}}(t)) \\
\Delta \dot{P}_{gi} &= \frac{K_{gi}}{T_{gi}} \left(\mu_i - \Delta E_i - \frac{\Delta f_i}{R_i} - \Delta P_{gi} \right) \\
\Delta \dot{P}_{PV_i} &= \frac{1}{T_{PV_i}} (-\Delta P_{PV_i} + \Delta P_{\phi_i} K_{PV_i}) \\
\Delta \dot{P}_{WT_i} &= \frac{1}{T_{WT_i}} (K_{wi} \Delta P_{\text{wind-i}} - \Delta P_{WT_i})
\end{aligned} \tag{1}$$

in which $f_i(t) = -\frac{D_i}{2H_i} \Delta f_i(t)$, $P_{mi} = \frac{1}{2H_i} \Delta P_{mi}(t)$, $P_{PV_i} = \frac{1}{2H_i} \Delta P_{PV_i}$, $P_{WT_i} = \frac{1}{2H_i} \Delta P_{WT_i}(t)$, $P_{tie-ij} = -\frac{1}{2H_i} \Delta P_{tie-ij}(t)$, and $P_{Li} = -\frac{1}{2H_i} \Delta P_{Li}(t)$. β_i , R_i , T_{ij} , D_i , H_i , K_{ti} , T_{ti} , K_{gi} , T_{gi} , T_{PV_i} , and T_{wi} are system coefficients and time constants. Δf_i , Δf_j , ΔP_{mi} , ΔP_{PV_i} , ΔP_{WT_i} , ΔP_{Li} , ΔP_{gi} , and $\Delta P_{\text{wind-i}}$ are deviations or variations, μ_i is control signal, details are presented in [19, 20, 21, 22]. Now, Equation (1) can be rewritten in state-space form as:

$$\dot{x}_i = A_i x_i(t) + B_i u_i(t) + \sum_{i=1, i \neq j}^n A_{ij} x_j(t) + \psi_i \Delta P_{di} \tag{2}$$

in which $x_i = [\Delta P_{\text{tie-ij}} \Delta f_i \Delta P_{mi} \Delta E_i \Delta P_{gi} \Delta P_{PV_i} \Delta P_{WT_i}]^T$ is the state variables, $A_{ij} = \begin{pmatrix} a_{11} & 0_{1 \times 6} \\ 0_{6 \times 1} & 0_{6 \times 6} \end{pmatrix}$, with $a_{11} = -2\pi \sum_{i=1, i \neq j}^n T_{ij}$,

$$A_i = \begin{pmatrix} 0 & \gamma_i & 0 & 0 & 0 & 0 & 0 \\ -\frac{1}{2H_i} & -\frac{D_i}{2H_i} & \frac{1}{2H_i} & 0 & 0 & \frac{1}{2H_i} & \frac{1}{2H_i} \\ 0 & 0 & -\frac{K_{ti}}{T_{ti}} & 0 & \frac{K_{ti}}{T_{ti}} & 0 & 0 \\ K_{Ei} & K_{Ei} \beta_i & 0 & 0 & 0 & 0 & 0 \\ 0 & -\frac{K_{gi}}{R_i T_{gi}} & 0 & -\frac{K_{gi}}{T_{gi}} - \frac{K_{gi}}{T_{gi}} & 0 & 0 & 0 \\ 0 & 0 & 0 & 0 & 0 & -\frac{1}{T_{PV_i}} & 0 \\ 0 & 0 & 0 & 0 & 0 & 0 & -\frac{1}{T_{WT_i}} \end{pmatrix}$$

with $\gamma_i = 2\pi \sum_{i=1, i \neq j}^n T_{ij}$, $B_i = [0 \ 0 \ 0 \ 0 \ \frac{K_{gi}}{T_{gi}} \ 0 \ 0]^T$,

$$\psi_i = \begin{pmatrix} 0 & 0 & 0 \\ -\frac{1}{2H_i} & 0 & 0 \\ 0 & 0 & 0 \\ 0 & 0 & 0 \\ 0 & \frac{K_{PV_i}}{T_{PV_i}} & 0 \\ 0 & 0 & \frac{K_{WT_i}}{T_{WT_i}} \end{pmatrix}$$

and $\Delta P_{di} = [\Delta P_{Li} \ \Delta P_{\phi_i} \ \Delta P_{\text{wind-i}}]^T$.

Matrices A_i , A_{ij} , B_i , and ψ_i in Equation (2) are assumed known, but real-world variations in frequency, tie-line power, and generation, along with load fluctuations and system reconfigurations, introduce modeling uncertainties. Thus, the power system dynamics under uncertainty is [20, 21]:

$$\dot{x}_i = (A_{0i} + \Delta A_i) x_i + (B_{0i} + \Delta B_i) \mu_i + \sum_{i=1, i \neq j}^n (A_{0ij} + \Delta A_{ij}) x_j + (\psi_{0i} + \Delta \psi_i) \Delta P_{di} \tag{3}$$

where A_{0i}, B_{0i}, A_{0ij} , and ψ_{0i} stand the nominal system matrices, and $\Delta A_i, \Delta B_i, \Delta A_{ij}, \Delta \psi_i$ denote the uncertainties. Then, Equation (3) becomes:

$$\dot{x}_i = A_i x_i(t) + B_i \mu_i(t) + \sigma_i \quad (4)$$

where $\sigma_i = \Delta A_i + \Delta B_i \Delta \mu_i + \sum_{i=1, i \neq j}^n (A_{ij} + \Delta A_{ij}) x_j + (\psi_i + \Delta \psi_i) \Delta P_{di}$ represents the lumped perturbation. In Equation (4), the dimensions are $x_i \in \mathbb{R}^{n \times 1}, A_i \in \mathbb{R}^{n \times n}, B_i \in \mathbb{R}^{n \times m}, \mu_i \in \mathbb{R}^{m \times 1}$, and $\sigma_i \in \mathbb{R}^{n \times 1}$.

Assumption 1. The lumped disturbance is bounded, i.e., $\|\sigma_i\| \leq \zeta_i$, where $\zeta_i > 0$ is known.

3 Design of the Proposed Robust GITSMC with an Exponential Reaching Law

In this section, a robust GITSMC is developed to guarantee finite-time convergence of the system output to equilibrium. To mitigate lumped perturbations, enhance transient performance, eliminate steady-state error, and reduce chattering, a global integral terminal sliding surface [23] ($\Theta_i(t) \in \mathbb{R}^{m \times 1}$) is proposed as follows:

$$\Theta_i(t) = \vartheta_i x_i(t) + \vartheta_i \lambda_{1i} \int x(t) dt + \vartheta_i \lambda_{2i} \int (x^{\alpha_i}(t)) dt \quad (5)$$

where $\lambda_{1i}, \lambda_{2i}$ and α_i ($1 < \alpha_i < 2$) are user-defined constant. The matrix $\vartheta_i \in \mathbb{R}^{m \times n}$ should be selected to ensure that the product $\vartheta_i B_{0i}$ is non-singular. The time derivative of $\Theta_i(t)$ incorporating Equation (4) is:

$$\dot{\Theta}_i(t) = \vartheta_i A_{0i} x_i(t) + \vartheta_i B_{0i} \mu_i(t) + \vartheta_i \sigma_i + \vartheta_i \lambda_{1i} x(t) + \vartheta_i \lambda_{2i} (x^{\alpha_i}(t)) \quad (6)$$

Setting $\dot{\Theta}_i(t) = 0$, we have:

$$0 = \vartheta_i A_{0i} x_i(t) + \vartheta_i B_{0i} \mu_i(t) + \vartheta_i \sigma_i + \vartheta_i \lambda_{1i} x(t) + \vartheta_i \lambda_{2i} (x^{\alpha_i}(t)) \quad (7)$$

Thus, neglecting the uncertainties in Equation (7), the equivalent control law is:

$$\mu_{eqi}(t) = -\frac{1}{\vartheta_i B_{0i}} (\vartheta_i A_{0i} x_i(t) + \vartheta_i \sigma_i + \vartheta_i \lambda_{1i} x(t) + \vartheta_i \lambda_{2i} x^{\alpha_i}(t)) \quad (8)$$

An exponential reaching law [23] is deployed to suppress the chattering and achieve fast finite-time convergence, as follows:

$$\mu_{swi}(t) = -\frac{1}{\vartheta_i B_{0i}} \left(\eta_{1i} \Theta_i(t) + \eta_{2i} \frac{\Theta_i(t)}{\|\Theta_i\|} \right) \quad (9)$$

where $\eta_{1i} > 0, \eta_{2i} > 0 \in \mathbb{R}^{1 \times m}$ are user-defined switching matrices. Accordingly, the overall control law $\mu_i(t)$ based on the SMC principle is given by:

$$\mu_i(t) = \mu_{eqi}(t) + \mu_{swi}(t) \quad (10)$$

The overall control law incorporating Equation (8) and Equation (9) is:

$$\mu_i(t) = -\frac{1}{\vartheta_i B_{0i}} (\vartheta_i A_{0i} x_i + \vartheta_i \lambda_{1i} x(t) + \vartheta_i \sigma_i + \vartheta_i \lambda_{2i} x^{\alpha_i}) - \frac{1}{\vartheta_i B_{0i}} \left(\eta_{1i} \Theta_i + \eta_{2i} \frac{\Theta_i}{\|\Theta_i\|} \right) \quad (11)$$

Now, Equation (6) becomes:

$$\dot{\Theta}_i(t) = -\eta_{1i} \Theta_i(t) - \eta_{2i} \frac{\Theta_i(t)}{\|\Theta_i\|} + \vartheta_i \sigma_i(t) \quad (12)$$

The Lyapunov control function is chosen as follows to verify the overall system stability:

$$L_i(t) = \frac{1}{2} \Theta_i^2 \quad (13)$$

Remark 1. If the Lyapunov function $L_i(t)$ is positive-definite, then the system is said to be asymptotically stable and should meet the conditions: $L_i(t) > 0 \forall \Theta_i(t) \neq 0, \dot{L}_i(t) \leq 0$, and $L_i(0) = 0$.

The time derivative of $L_i(t)$ based on Equation (12) is:

$$\dot{L}_i(t) = \Theta_i(t) \left(-\eta_{1i} \Theta_i(t) - \eta_{2i} \frac{\Theta_i(t)}{\|\Theta_i\|} + \vartheta_i \sigma_i(t) \right) \quad (14)$$

which becomes:

$$\dot{L}_i(t) \leq -\|\eta_{1i} \Theta_i^2\| - \frac{\|\eta_{2i} \Theta_i^2\|}{\|\Theta_i\|} + \|\vartheta_i \sigma_i \Theta_i\| \quad (15)$$

We can rewrite Equation (15) applying the inequality $||mn|| \leq ||m|| ||n||$ as:

$$\dot{L}_i(t) \leq -||\eta_{1i}|| ||\Theta_i^2|| - \frac{||\eta_{2i}|| ||\Theta_i^2||}{||\Theta_i||} + ||\vartheta_i|| ||\sigma_i|| ||\Theta_i|| \quad (16)$$

which becomes:

$$\dot{L}_i(t) \leq -||\eta_{1i}|| ||\Theta_i^2|| - ||\eta_{2i}|| ||\Theta_i|| + ||\vartheta_i|| ||\sigma_i|| ||\Theta_i|| \quad (17)$$

Under *Assumption 1*, Equation (17) simplifies to:

$$\dot{L}_i(t) \leq -||\eta_{1i}|| ||\Theta_i^2|| - ||\Theta_i|| (||\eta_i|| - ||\vartheta_i|| \mu_i) \quad (18)$$

As $||\eta_{1i}|| > 0$ and $||\eta_{2i}|| \geq ||\vartheta_i|| \zeta_i$, we have $\dot{L}_i(t) \leq 0$. Therefore, from Equation (18), the overall LFC system under the control law Equation (11) is stable, and the sliding surface converges to zero in finite time despite aggregated uncertainties. The finite time convergence analysis is briefly given in Appendix A.

The next section presents numerical and comparative results evaluating the proposed control method.

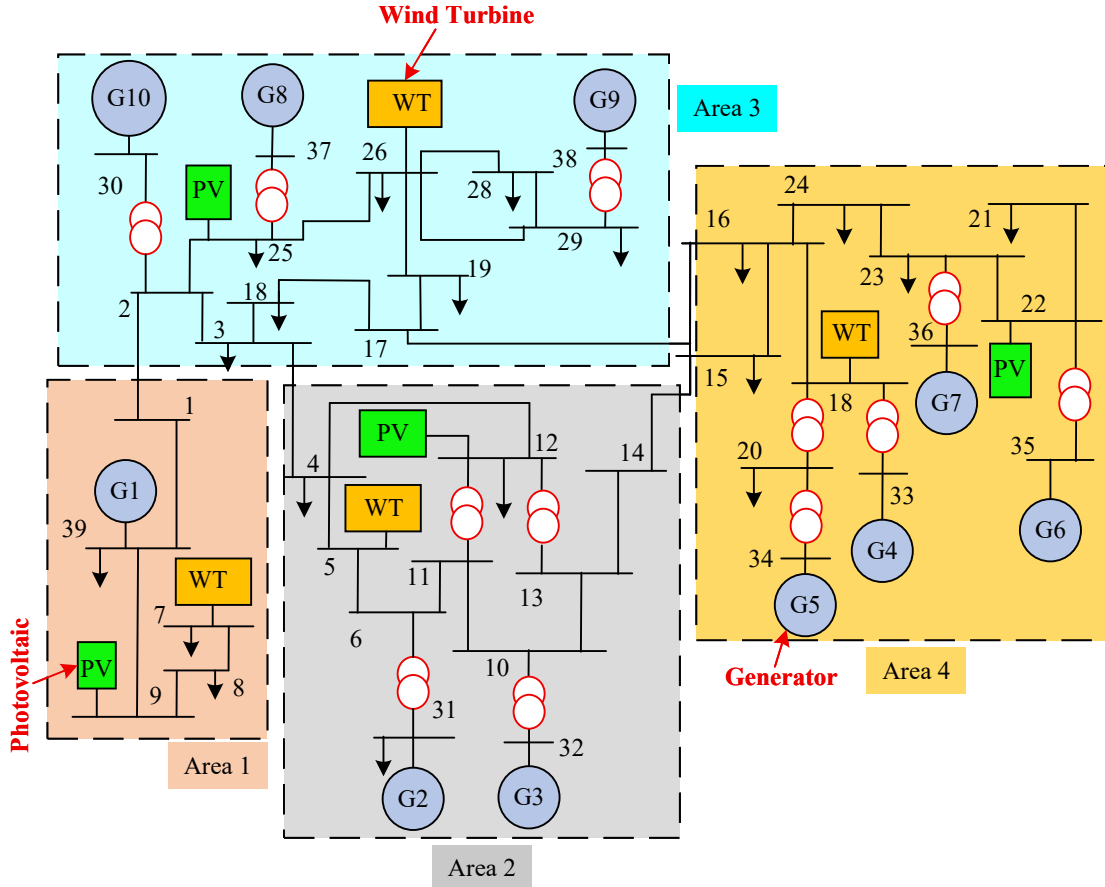


Figure 2: Single line illustration of the IEEE 10-generator New England 39-bus power system [20, 21, 24, 25].

4 Results and Analysis

The IEEE 10-generator New England 39-bus power network [20, 21, 24, 25], as given in Figure 2, is deployed to evaluate the efficacy of the constructed decentralized GITSMC scheme. This widely adopted test system is frequently employed in dynamic stability analyses and is partitioned into four interconnected subareas. This IEEE 39-bus system is subdivided into four different areas. Area 1 comprises generator G_1 . Area 2 includes generators G_2 and G_3 , while area 3 consists of generators G_8 , G_9 , and G_{10} . The generators G_4 – G_7 are assigned to area 4. Each area is also equipped with a PV unit, a WT unit, and step load disturbances. The power system's net installed capacity amounts to 6408

Table 1: Parameters of the IEEE 39-bus (New England) power network [20, 21, 24, 25]

Area	Generator	S	T_t	T_g	R	H	T_{ij}
1	G_1	1000	0.3742	0.0804	0.0471	10	$T_{13}=1.3272$
	G_2	520.81	0.3888	0.0774	0.0541	6.06	$T_{23}=0.2959$
2	G_3	650	0.3645	0.0748	0.0518	7.16	$T_{24}=0.6128$
	G_4	632	0.3707	0.0759	0.0540	5.72	$T_{31}=1.3272$
	G_5	508	0.3770	0.0729	0.0470	5.20	$T_{32}=0.2959$
	G_6	650	0.4316	0.0791	0.0459	6.96	$T_{34}=0.3959$
3	G_7	560	0.3657	0.0722	0.0481	5.28	
	G_8	540	0.3665	0.0805	0.0484	4.86	$T_{42}=0.6128$
	G_9	830	0.4222	0.0737	0.0479	6.90	$T_{43}=0.3959$
4	G_{10}	250	0.4324	0.0852	0.0525	8.40	

$D = 1$ for all the generators

Table 2: Model parameters for the load frequency control scheme [20, 21, 24, 25]

Area	$T_{t\text{-equiv}}$	$T_{g\text{-equiv}}$	R_{equiv}	β	H_{equiv}	T_{ij}
1	0.3742	0.0804	0.0471	22.2314	10	T_{13}
2	0.3766	0.0760	0.0528	6.6706	19.9394	T_{23}, T_{24}
3	0.3862	0.0750	0.0486	21.5761	6.6706	T_{31}, T_{32}, T_{34}
4	0.4070	0.0798	0.0487	21.5339	6.4515	T_{42}, T_{43}

$T_{13} = T_{31} = 1.3272$, $T_{23} = T_{32} = 0.2959$, $T_{24} = T_{42} = 0.6128$, $T_{43} = 0.3959$, and $D_{\text{equiv}} = 1$ in all areas.

MVA, with load demands of 959 MW, 1867 MW, 2350 MW, and 1707.5 MW corresponding to areas 1–4, respectively. As shown in Figure 2, the tie-line links between the subareas are arranged as follows: area 1 is connected to area 3 through buses 1–2; area 2 is linked to area 3 via buses 3–4; area 2 connects to area 4 through buses 14–15; and area 3 is tied to area 4 at buses 16–17. Four WT units, each rated at 100 MW and totaling 400 MW, are connected to buses 5, 7, 18, and 26. Similarly, four solar PV units, also rated at 100 MW each and totaling 400 MW, are integrated at buses 9, 12, 22, and 25. Consequently, the combined renewable generation from WT and PV sources equals 800 MW, corresponding to a per-unit value of 0.8. Moreover, Table 1 presents the tie-line synchronizing torque coefficients for this four-area power system [26]. Table 2 provides an overview of the parameters utilized in developing the proposed four-area LFC model. Using the data from Table 2, the matrices for the interconnected power systems in the four areas are calculated, and they are presented in Appendix B. The simulation data for a PV unit is $T_{PV} = 1.8$, and $K_{PV} = 1$; and for a WT is $T_{WT} = 1.5$, and $K_{WT} = 1$. The effectiveness of the proposed controller is assessed by incorporating step load disturbances along with the presence of WT and PV power generators in all areas. In this paper, the performance of the designed decentralized robust GITSMC is compared with that of a classical PI controller. For the simulation the following control parameters of the proposed GITSMC are used: $\alpha_1 = \alpha_2 = \alpha_3 = \alpha_4 = 1.7$, $\lambda_1 = \lambda_2 = \lambda_3 = \lambda_4 = 24$, $\eta_{11} = \eta_{12} = \eta_{13} = \eta_{14} = [1.498 \ 1.991 \ 0.637 \ 0.728 \ 0.1582 \ 0.248 \ 0.239]$, and $\eta_{21} = \eta_{22} = \eta_{23} = \eta_{24} = [2.498 \ 2.991 \ 0.737 \ 0.728 \ 0.258 \ 0.148 \ 0.339]$.

The performance of the controllers is evaluated under step load disturbances applied to all four areas. Specifically, a 0.5 pu step load is introduced in area 1 at $t = 50$ s and removed at $t = 250$ s. In area 2, a 1 pu step load is applied at $t = 150$ s and cleared at $t = 250$ s, while in areas 3 and 4, a 1 pu step load is applied at $t = 250$ s and terminated at $t = 300$ s and $t = 350$ s, respectively, as illustrated in Fig. 3. In addition, the PV and WT generation variations, shown in Fig. 3, are considered in all four areas. The PV power remains at 0 pu from $t = 0$ –50 s and $t = 300$ –400 s, and increases to 0.25 pu during $t = 50$ –300 s. The wind power is 0.8 pu for $t = 0$ –100 s, rises to 0.9 pu during $t = 100$ –270 s, and drops to 0 pu for $t = 270$ –400 s.

Remark 2. Since variations in WT output power, PV generation, and load demand naturally occur in practical power systems, these disturbances are incorporated to rigorously assess the effectiveness of the proposed controller.

The frequency deviation and tie-line power for all areas are shown in Figure 4 and Figure 5, respectively. Figure 4 illustrates the effect of step load disturbances on the system frequency. When the load increases, the frequency drops noticeably. The proposed GITSMC controller performs better than the classical PI controller in managing these disturbances. It achieves smaller overshoot and undershoot, along with a faster settling time, showing its improved

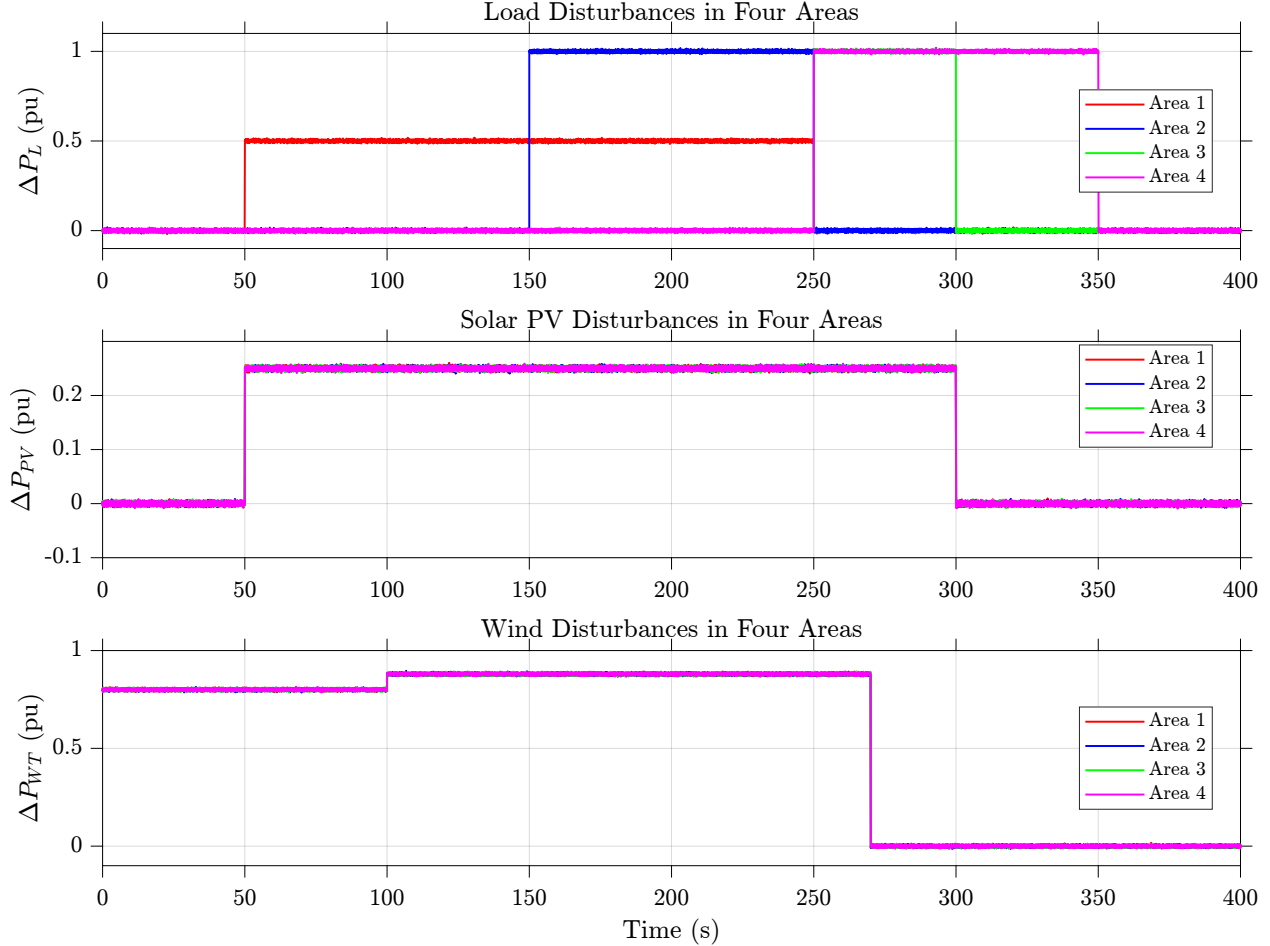


Figure 3: Step load, PV, and wind disturbances are applied across the four interconnected areas to emulate realistic operating conditions for evaluating the proposed GITSMC. Each disturbance includes added zero-mean constant variance Gaussian noise.

ability to reduce the effects of sudden load changes, variable PV, and WT power. Similar behavior is seen in the tie-line power deviation in Figure 5. With the proposed control method, the tie-line power quickly stabilizes, and the oscillations are effectively reduced during load, PV, and WT disturbances.

The integral performance indices, given in Appendix C, reveal that the proposed GITSMC controller outperforms the conventional PI controller. Although the GITSMC controller achieves ITAE and IAE values of 3.144011×10^{-1} and 1.499759×10^{-3} , which are slightly larger than those of the PI controller (3.116500×10^{-1} and 1.379475×10^{-3}), the differences remain within acceptable limits, indicating comparable transient performance. While the ITAE and IAE values for the GITSMC controller are slightly higher than those of the PI controller, it shows marked improvement in squared-error metrics, with integral time-weighted squared error (ITSE) and integral squared error (ISE) values of 4.430051×10^{-7} and 1.914747×10^{-9} , respectively, compared to 8.712740×10^{-6} and 3.441012×10^{-8} for the PI controller. These outcomes unequivocally present that the proposed GITSMC provides pronounced reductions in squared-error energy, indicative of more effective damping, suppressed oscillations, and reinforced disturbance rejection, despite a modest rise in the integral of absolute errors.

5 Conclusion & Future Research

We propose a global integral terminal sliding mode controller (GITSMC) to enhance load frequency control in multi-area interconnected power systems with PV and wind energy integration. The proposed controller employs a global integral terminal sliding surface to achieve finite-time convergence and robust performance under dynamic operating conditions. An exponential reaching law is introduced to suppress chattering, and Lyapunov-based analysis confirms the overall system stability. Simulation results under step load and renewable power variations demonstrate that the proposed controller outperforms the classical PI controller, achieving quicker settling time with decreased overshoot

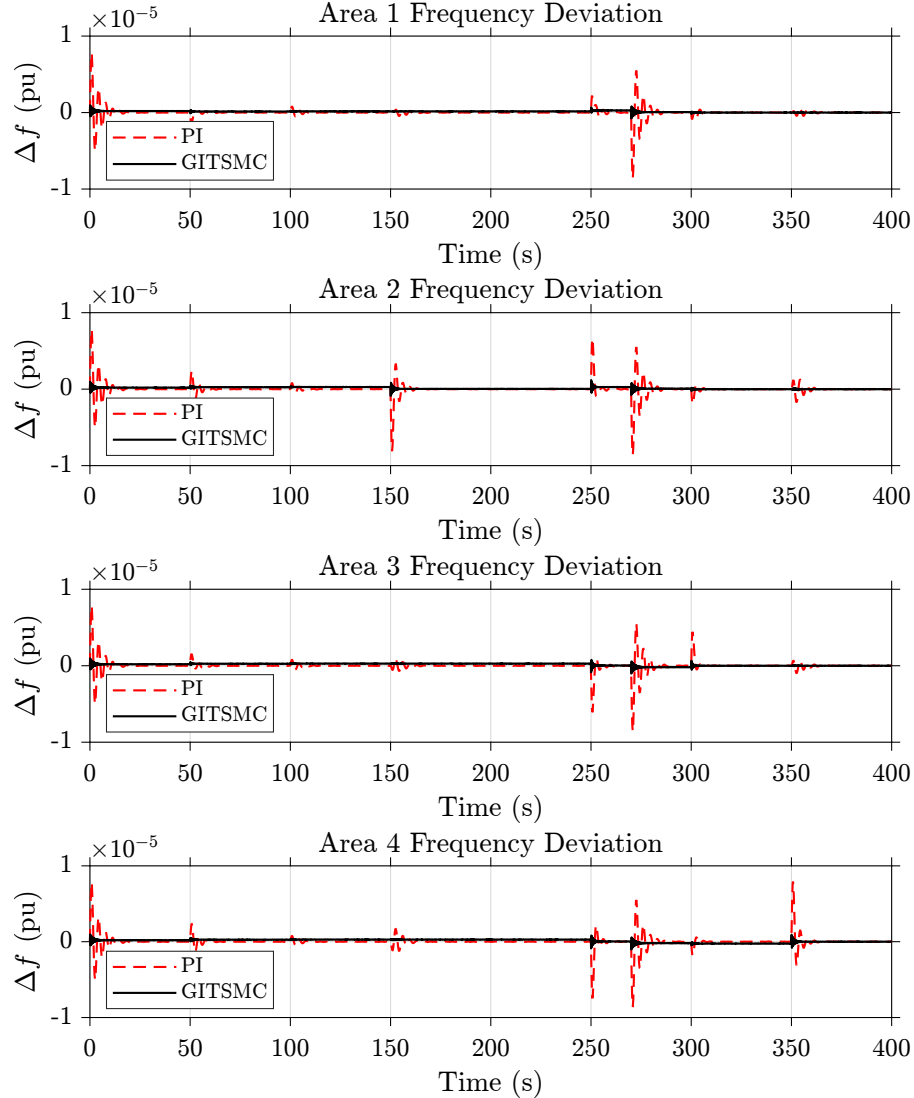


Figure 4: Frequency deviations under variable PV, WT power, and step load fluctuations. The proposed GITSMC shows faster settling and smaller overshoot/undershoot compared to the PI controller.

and undershoot in frequency and tie-line power responses. Furthermore, the GITSMC achieves approximately 94.9% enhancement in ITSE and 94.4% enhancement in ISE, validating its superior accuracy, robustness, and adaptability in modern power systems.

Future work may focus on developing robust adaptive and virtual inertia controllers to enhance stability under high renewable penetration. Additionally, incorporating machine learning-based and quantum computing-based controllers could further enhance adaptability and optimization in complex power systems. We will also validate the implementation of our controller with a real-world equivalent hardware-in-the-loop simulation in laboratory settings, with a goal of field testing at a later stage.

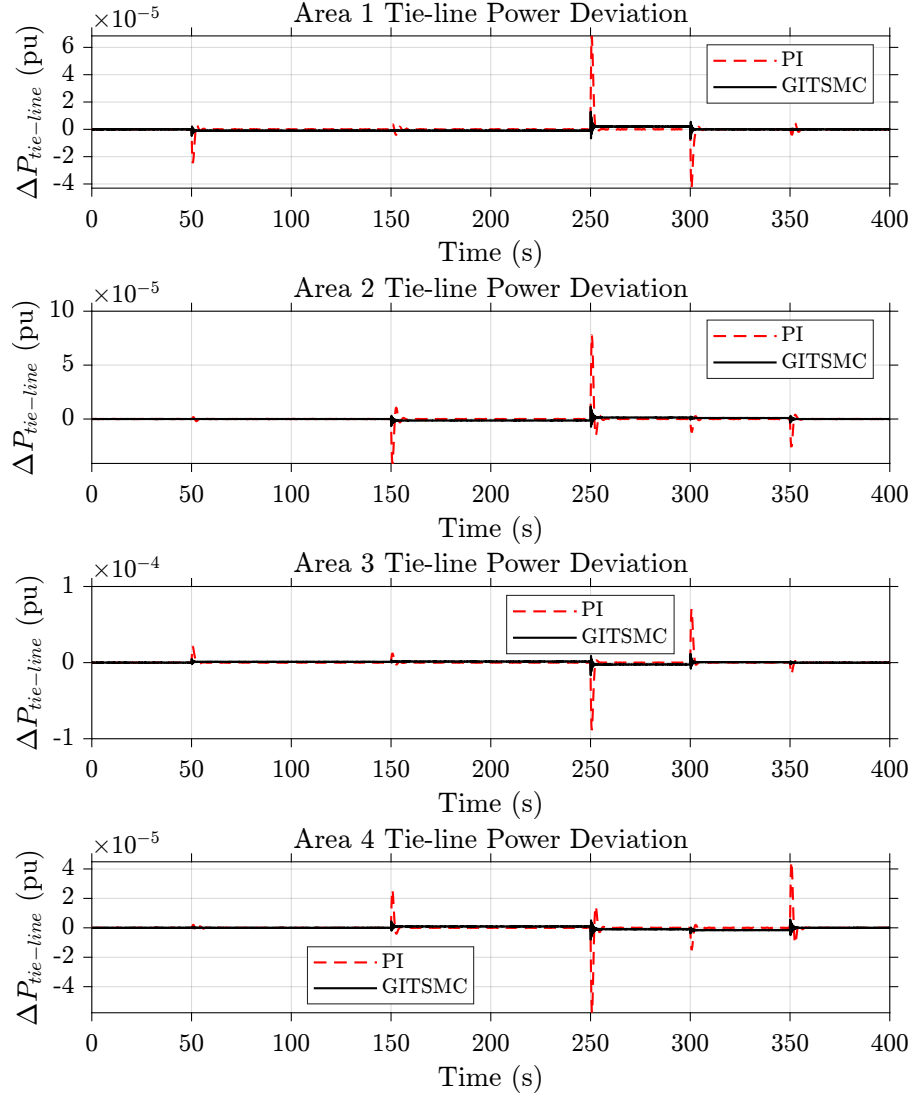


Figure 5: Tie-line power deviations under load, PV, and WT disturbances. The proposed GITSMC stabilizes the tie-line power quicker and decreases the oscillations compared to the PI controller.

References

- [1] Md Saiful Islam, Israt Jahan Bushra, Tushar Kanti Roy, Subarto Kumar Ghosh, and Amanullah Maung Than Oo. Enhanced composite controller for PV/PMSG/PEMFC and BESS-based DC microgrids voltage regulation: Integrating integral terminal sliding mode controller and recursive backstepping controller. *IET Generation, Transmission & Distribution*, 18(22):3608–3632, 2024.
- [2] Md Saiful Islam, Israt Jahan Bushra, Tushar Kanti Roy, and Amanullah Maung Than Oo. Enhanced transient stability in hybrid DC/AC microgrids: Robust composite control strategy with virtual capacitors integration using ANFIS-optimized control gain parameters. *IET Renewable Power Generation*, 19(1):e70066, 2025.
- [3] Md Saiful Islam, Tushar Kanti Roy, and Israt Jahan Bushra. Marine predators algorithm-based robust composite controller for enhanced power sharing and real-time voltage stability in DC–AC microgrids. *Algorithms*, 18(8):531, 2025.
- [4] Jie Feng, Wenqi Cui, Jorge Cortés, and Yuanyuan Shi. Online event-triggered switching for frequency control in power grids with variable inertia. *IEEE Transactions on Power Systems*, 2025.
- [5] Itishree Ghatuari and N Senthil Kumar. A coordinated control strategy of electric vehicles for frequency control in modern power grids. *IEEE Access*, 2025.

[6] Jan Machowski, Janusz W Bialek, Janusz Bialek, and James Richard Bumby. *Power system dynamics and stability*. John Wiley & Sons, 1997.

[7] Xing-Chen Shangguan, Yuan-Hang Yang, Yong He, Chen-Guang Wei, Chuan-Ke Zhang, and Lin Jiang. Dissipativity-based integral-sliding-mode load frequency control considering disturbances and denial-of-service attacks. *IEEE Transactions on Power Systems*, 2025.

[8] Dip Kumar Biswas, Sanjoy Debbarma, and Piyush Pratap Singh. Dynamic surface sliding mode control-based LFC design for RES-dominated power systems with a provision of grid-scale virtual energy storage. *IEEE Transactions on Power Systems*, 2025.

[9] Thomas John. Operation and control of multi-area multi-microgrid systems, 2017.

[10] Yonghui Sun, Yingxuan Wang, Zhinong Wei, Guoqiang Sun, and Xiaopeng Wu. Robust H_∞ load frequency control of multi-area power system with time delay: a sliding mode control approach. *IEEE/CAA Journal of Automatica Sinica*, 5(2):610–617, 2017.

[11] Bin Guo, Songyi Dian, Ben Niu, Yuqi Zhu, and Tao Zhao. Observer-based compensation control for nonlinear interconnected power systems with load disturbances and actuator faults. *IEEE Transactions on Automation Science and Engineering*, 2025.

[12] Dipayan Guha, Provas Kumar Roy, and Subrata Banerjee. Improved fractional-order sliding mode controller for frequency regulation of a hybrid power system with nonlinear disturbance observer. *IEEE Transactions on Industry Applications*, 59(4):4964–4979, 2023.

[13] Xue Yu, Gang Wang, Yuan Zhong, Huaguang Zhang, and Jinhai Liu. Predictor-based fractional-order sliding mode LFC for interconnected power systems with input delay. *IEEE Transactions on Cybernetics*, 2025.

[14] Jiaming Qian and Xinxin Lv. Load frequency control of renewable energy power systems based on adaptive global fast terminal sliding mode control. *Applied Sciences*, 15(13):7030, 2025.

[15] Nan Zhang, Zheren Zhang, and Zheng Xu. A coordinated adaptive SMC method for frequency regulation control in power systems with multiple wind farms. *IEEE Transactions on Sustainable Energy*, 2025.

[16] Issarachai Ngamroo and Sitthidet Vachirasricirikul. Design of optimal SMES controller considering SOC and robustness for microgrid stabilization. *IEEE Transactions on Applied Superconductivity*, 26(7):1–5, 2016.

[17] Ahmad Bala Alhassan and Ton Duc Do. The influence of higher-order disturbance estimation on wind power generation of WECS using SMC with sensorless wind speed estimation. *IEEE Access*, 2025.

[18] A Sharifi, K Sabahi, M Aliyari Shoorehdeli, MA Nekoui, and M Teshnehlab. Load frequency control in interconnected power system using multi-objective PID controller. In *2008 IEEE conference on soft computing in industrial applications*, pages 217–221. IEEE, 2008.

[19] Rabindra Kumar Sahu, Sidhartha Panda, and Pratap Chandra Pradhan. Design and analysis of hybrid firefly algorithm-pattern search based fuzzy PID controller for LFC of multi area power systems. *International Journal of Electrical Power & Energy Systems*, 69:200–212, 2015.

[20] Tushar Kanti Roy, Samson S Yu, Md Apel Mahmud, and Hieu Trinh. Robust LFC design using adaptive neuro-fuzzy inference-aided optimal fractional-order PIDA control for perturbed power systems with solar and wind power sources. *IET Generation, Transmission & Distribution*, 18(12):2193–2212, 2024.

[21] Tushar Kanti Roy, Md Apel Mahmud, and Amanullah Maung Than Oo. Multi-area load frequency control using an adaptive reaching law-based integral terminal sliding mode scheme. In *2024 IEEE International Conference on Power Electronics, Drives and Energy Systems (PEDES)*, pages 1–6. IEEE, 2024.

[22] Fan Yang, Xinyi Shao, SM Muyeen, Dongdong Li, Shunfu Lin, and Chen Fang. Disturbance observer based fractional-order integral sliding mode frequency control strategy for interconnected power system. *IEEE Transactions on Power Systems*, 36(6):5922–5932, 2021.

[23] Md Saiful Islam, Israt Jahan Bushra, Tushar Kanti Roy, and Jim Mortaej Chowdhury. Stability enhancement of DC microgrids under CPLs using secretary bird optimization algorithm-tuned backstepping-GITSM control: Design, simulation, and experimental approach. *IET Power Electronics*, 18(1):e70118, 2025.

[24] SK Jain, G Narayanan, et al. Real-time simulation of IEEE 10-generator 39-bus system with power system stabilizers on miniature full spectrum simulator. In *2019 IEEE International Conference on Sustainable Energy Technologies and Systems (ICSETS)*, pages 161–166. IEEE, 2019.

[25] Ziming Yan and Yan Xu. A multi-agent deep reinforcement learning method for cooperative load frequency control of a multi-area power system. *IEEE Transactions on Power Systems*, 35(6):4599–4608, 2020.

[26] Li Jin, Yong He, Chuan-Ke Zhang, Lin Jiang, Wei Yao, and Min Wu. Delay-dependent stability of load frequency control with adjustable computation accuracy and complexity. *Control Engineering Practice*, 135:105518, 2023.

A Finite Time Convergence Analysis

The finite convergence time (t_f) of the GITSMC controller for a nonzero initial state $x_i(0)$ is determined as follows. The sliding mode occurs when $\Theta_i(t) = 0$. From Equation (5), the system dynamics can be expressed as:

$$\dot{x}_i(t) = -\lambda_i x_i^{\alpha_i}(t) \quad (\text{A.1})$$

Rearranging:

$$dt = -\frac{dx_i}{\lambda_i x_i^{\alpha_i}} \quad (\text{A.2})$$

Integrating:

$$\int_0^{t_f} dt = - \int_{x_i(0)}^{x_i(t_f)} \frac{dx_i}{\lambda_i x_i^{\alpha_i}} \quad (\text{A.3})$$

Solving Equation (A.3) provides the finite-time convergence expression as:

$$t_f = \frac{|x_i(t_f)|^{1-\alpha_i} - |x_i(0)|^{1-\alpha_i}}{\lambda_i(\alpha_i - 1)} \quad (\text{A.4})$$

Hence, the system trajectory reaches the origin within a finite time, confirming the finite-time stability property.

B State-Space Matrices of the Four-Area Power System

Based on the parameters provided in Table 2, the state-space representations for the four areas are obtained as follows.

Area 1:

$$A_{01} = \begin{pmatrix} 0 & 8.33 & 0 & 0 & 0 & 0 & 0 \\ -5 & -5 & 5 & 0 & 0 & 5 & 5 \\ 0 & 0 & -2.67 & 0 & 2.67 & 0 & 0 \\ 5 & 11.15 & 0 & 0 & 0 & 0 & 0 \\ 0 & -264.07 & 0 & -12.43 & -12.43 & 0 & 0 \\ 0 & 0 & 0 & 0 & 0 & -25 & 0 \\ 0 & 0 & 0 & 0 & 0 & 0 & -23.81 \end{pmatrix}, \quad B_{01} = [0 \ 0 \ 0 \ 0 \ 12.43 \ 0 \ 0]^T,$$

$$\theta_1 = [0 \ 0 \ 0 \ 0 \ 1/12.43 \ 0 \ 0].$$

Area 2:

$$A_{02} = \begin{pmatrix} 0 & 5.70 & 0 & 0 & 0 & 0 & 0 \\ -3.33 & -3.33 & 3.33 & 0 & 0 & 3.33 & 3.33 \\ 0 & 0 & -2.65 & 0 & 2.65 & 0 & 0 \\ 5 & 99.69 & 0 & 0 & 0 & 0 & 0 \\ 0 & -279.36 & 0 & -13.15 & -13.15 & 0 & 0 \\ 0 & 0 & 0 & 0 & 0 & -25 & 0 \\ 0 & 0 & 0 & 0 & 0 & 0 & -23.81 \end{pmatrix}, \quad B_{02} = [0 \ 0 \ 0 \ 0 \ 13.15 \ 0 \ 0]^T,$$

$$\theta_2 = [0 \ 0 \ 0 \ 0 \ 1/13.15 \ 0 \ 0].$$

Area 3:

$$A_{03} = \begin{pmatrix} 0 & 12.68 & 0 & 0 & 0 & 0 & 0 \\ -2.92 & -2.92 & 2.92 & 0 & 0 & 2.92 & 2.92 \\ 0 & 0 & -2.58 & 0 & 2.58 & 0 & 0 \\ 5 & 107.88 & 0 & 0 & 0 & 0 & 0 \\ 0 & -423.37 & 0 & -13.33 & -13.33 & 0 & 0 \\ 0 & 0 & 0 & 0 & 0 & -25 & 0 \\ 0 & 0 & 0 & 0 & 0 & 0 & -23.81 \end{pmatrix}, \quad B_{03} = [0 \ 0 \ 0 \ 0 \ 20.57 \ 0 \ 0]^T,$$

$$\theta_3 = [0 \ 0 \ 0 \ 0 \ 1/20.57 \ 0 \ 0].$$

Area 4:

$$A_{04} = \begin{pmatrix} 0 & 6.33 & 0 & 0 & 0 & 0 & 0 \\ -3.22 & -3.22 & 3.22 & 0 & 0 & 3.22 & 3.22 \\ 0 & 0 & -2.45 & 0 & 2.45 & 0 & 0 \\ 5 & 107.66 & 0 & 0 & 0 & 0 & 0 \\ 0 & -257.31 & 0 & -12.53 & -12.53 & 0 & 0 \\ 0 & 0 & 0 & 0 & 0 & -25 & 0 \\ 0 & 0 & 0 & 0 & 0 & 0 & -23.81 \end{pmatrix}, \quad B_{04} = [0 \ 0 \ 0 \ 0 \ 12.53 \ 0 \ 0]^T,$$

$$\theta_4 = [0 \ 0 \ 0 \ 0 \ 1/12.53 \ 0 \ 0].$$

Appendix C. Integral Indices

The following integral indices are utilized to evaluate the dynamic performance of the proposed controller in terms of frequency and tie-line power deviations across the interconnected areas [20, 21].

$$\text{ITAE} = \int_0^t \left(\sum_{i=1, i \neq j}^n (|\Delta f_i| + |\Delta P_{\text{tie-line } ij}|) \right) t dt \quad (\text{C.1})$$

$$\text{ITSE} = \int_0^t \left(|\Delta f_i|^2 + |\Delta P_{\text{tie-line } ij}|^2 \right) t dt \quad (\text{C.2})$$

$$\text{ISE} = \int_0^t \left(|\Delta f_i|^2 + |\Delta P_{\text{tie-line } ij}|^2 \right) dt \quad (\text{C.3})$$

$$\text{IAE} = \int_0^t \left(\sum_{i=1, i \neq j}^n (|\Delta f_i| + |\Delta P_{\text{tie-line } ij}|) \right) dt \quad (\text{C.4})$$